npj | computational materials

Review

Published in partnership with the Shanghai Institute of Ceramics of the Chinese Academy of Sciences

https://doi.org/10.1038/s41524-025-01715-1

Technical review: Time-dependent density functional theory for attosecond physics ranging from gas-phase to solids

Shunsuke A. Sato[1,2,3] ✉, Hannes Hübener[3] ✉, Umberto De Giovannini[3,4] ✉ & Angel Rubio[3,5] ✉

First-principles electron dynamics calculations can be applied in the investigation of a wide range of ultrafast phenomena in attosecond physics. They offer unique microscopic insight into light-induced ultrafast phenomena in both gas and condensed phases of matter, and thus, they are a powerful tool to develop our understanding of the physics of attosecond phenomena. We specifically review techniques employing time-dependent density functional theory (TDDFT) for investigating attosecond and strong-field phenomena. First, we describe this theoretical framework that enables the modeling of perturbative and non-perturbative electron dynamics in materials, including atoms, molecules, and solids. We then discuss its application to attosecond experiments, focusing on the reconstruction of attosecond beating by interference of two-photon transitions (RABBIT) measurements. We also briefly review first-principles calculations of optical properties of solids with TDDFT in the linear response regime and their extension to calculations of transient optical properties of solids in non-equilibrium phases, by simulating experimental pump-probe setups. We further demonstrate the application of TDDFT simulation to high-order harmonic generation in solids. First-principles calculations have predictive power, and hence they can be utilized to design future experiments to explore non-equilibrium and nonlinear ultrafast phenomena in matter and characterize and control metastable light-induced quantum states.

After the invention of the laser by Schawlow and Townes in 1958[1] and the first observation of nonlinear optical effects[2], laser technology has significantly developed up to the present day[3,4]. A crucial breakthrough in laser technology was the development of the chirped pulse amplification technique, which significantly advanced the intensity of laser pulses[5]. This advancement has enabled reaching high field strengths comparable to the Coulomb force acting on electrons from ions within matter. This high field strength further triggered the discovery of an important, highly nonlinear optical phenomenon in the non-perturbative regime: high-order harmonic generation (HHG)[6,7]. HHG is an extreme photon-up-conversion process understood by the semi-classical three-step model, establishing a coherent radiation technique of attosecond light pulses[8,9].

The Nobel Prize in Physics of 2023 has been awarded for the experimental methods for generating attosecond light pulses, which opened a novel avenue for investigating electron dynamics in matter[10] known as *attosecond physics*. The foundation of attosecond physics may be constituted by three major developments: The first one is the observation of the plateau of high harmonics[7], indicating a nonperturbatively nonlinear microscopic process. Another important step is the demonstration of the generation of attosecond pulse trains by precisely measuring their width in the time domain via the reconstruction of attosecond beating by interference of two-photon transitions (RABBIT) technique[11]. The other major step is the generation of an isolated attosecond pulse with a few-cycle laser pulse[12]. Thanks to this revolutionary development, our understanding of ultrafast, nonlinear, and non-equilibrium electron dynamics in matter has significantly expanded over the past two decades[13,14]. For instance, the measurement of photoionization delay in gas phases has provided precise insights into the tunneling ionization process of isolated systems under strong fields[15–18]. Moreover, the application of the attosecond streaking technique has offered a dynamic picture of energy transfer from light to matter in the time domain[19]. Attosecond transient absorption and reflectivity measurements in solids have unveiled the roles of intraband and

[1]Department of Physics, Tohoku University, Sendai, Japan. [2]Center for Computational Sciences, University of Tsukuba, Tsukuba, Japan. [3]Max Planck Institute for the Structure and Dynamics of Matter and Center for Free Electron Laser Science, Hamburg, Germany. [4]Università degli Studi di Palermo, Dipartimento di Fisica e Chimica—Emilio Segrè, Palermo, Italy. [5]Center for Computational Quantum Physics (CCQ), Flatiron Institute, New York, NY, USA.
✉e-mail: shunsuke.sato@tohoku.ac.jp; hannes.huebener@mpsd.mpg.de; umberto.de-giovannini@mpsd.mpg.de; angel.rubio@mpsd.mpg.de

interband transitions in light-induced electron dynamics in solids[20,21], as well as many-body effects such as screening and excitonic effects[22–24]. Beyond advancing our understanding of ultrafast phenomena, attosecond laser technologies have also enabled important techniques such as laser-induced electron diffraction[25–28] and attosecond electron pulse generation[29–32]. Furthermore, this expanded knowledge is expected to play a key role in unlocking ultrafast technologies, such as Petahertz electronics[33–38].

However, experiments, especially in attosecond physics, observe macroscopic quantities such as spectra of photons or electrons, and the corresponding experimental results are often difficult to understand from the microscopic point of view because non-equilibrium complex nonlinear electron dynamics are at the origin of the observed phenomena. In this context, first-principles electron dynamics calculations based on time-dependent density functional theory (TDDFT) became a powerful tool for analyzing such microscopic electron dynamics[39–46]. First-principles electron dynamics simulations have been applied to attosecond experiments and have provided a microscopic understanding of light-induced ultrafast phenomena in atoms, molecules, and solids[20–22,47–52]. Furthermore, such simulations can be used to predict and design future experiments to explore fundamental questions concerning out-of-equilibrium electron dynamics, electronic correlation, and electron-phonon coupling effects in quantum matter.

In this review, we discuss first-principles electron dynamics calculations, especially focusing on applications to attosecond experiments for both gas and solid-state systems. After revisiting the basic principles of electron dynamics calculations using TDDFT, we introduce the application to time-resolved photoelectron spectroscopy, focusing on the RABBIT measurements[11]. We then discuss first-principle calculations for attosecond transient absorption spectroscopy, demonstrating the transient optical properties of magnets, bulk materials, and providing microscopic insights into the laser-induced electron dynamics in magnets. Furthermore, we introduce first-principles calculations for HHG from solids, aiming to establish novel light sources beyond the attosecond pulse generation relying on the HHG from gases. Hence, this review introduces the first-principles approach for both electron and photon spectra resulting from recent attosecond and strong-field experiments. Finally, we describe conclusions and provide perspectives on the first-principles simulations for attosecond physics.

Basic equation of motion: Time-dependent Kohn-Sham equation

Here, we briefly introduce the basic equation of motion of TDDFT, the so-called time-dependent Kohn-Sham equation, to describe electron dynamics in matter driven by arbitrary time-dependent and spatially dependent electromagnetic fields. The time-dependent Kohn-Sham equation[39] has the same form as the one-body time-dependent Schrödinger equation as

$$i\hbar\frac{\partial}{\partial t}\psi_j(\boldsymbol{r},t)=\hat{h}_{\mathrm{KS}}(t)\psi_j(\boldsymbol{r},t), \tag{1}$$

where $\psi_j(\boldsymbol{r},t)$ are single-electron orbitals, and $\hat{h}_{\mathrm{KS}}(t)$ is the effective one-body Hamiltonian, the so-called Kohn-Sham Hamiltonian. To describe light-induced electron dynamics, we employ the following form of the Kohn-Sham Hamiltonian in the long-wavelength approximation:

$$\begin{aligned}\hat{h}_{\mathrm{KS}}(t) &= \frac{1}{2m_e}\left[\hat{\boldsymbol{p}}+e\boldsymbol{A}(t)+e\boldsymbol{A}_{xc}(\boldsymbol{r},t)\right]^2\\ &\quad+e^{-ie\boldsymbol{A}(t)\cdot\boldsymbol{r}/\hbar}\hat{v}_{\mathrm{ion}}e^{ie\boldsymbol{A}(t)\cdot\boldsymbol{r}/\hbar}\\ &\quad+v_H(\boldsymbol{r},t)+v_{xc}(\boldsymbol{r},t),\end{aligned} \tag{2}$$

where $\boldsymbol{A}(t)$ is a spatially-uniform time-dependent vector potential, $\hat{v}_{\mathrm{ion}}$ is the ionic potential, $v_H(\boldsymbol{r},t)$ is the Hartree potential, $v_{xc}(\boldsymbol{r},t)$ is the exchange-correlation potential, and $\boldsymbol{A}_{xc}(\boldsymbol{r},t)$ is the exchange-correlation vector potential. In the dipole approximation, the optical electric field is described by a spatially-uniform electric field $\boldsymbol{E}(t)$, represented by the vector potential $\boldsymbol{A}(t)$ as $\boldsymbol{A}(t)=-\int_{-\infty}^{t}\mathrm{d}t'\boldsymbol{E}(t')$. The ionic potential $\hat{v}_{\mathrm{ion}}$ may involve a non-local operator through the norm-conserving pseudopotential approximation[53,54]. If the ionic potential contains spatially nonlocal parts through the pseudopotential approximation, the phase factor $e^{ie\boldsymbol{A}(t)\cdot\boldsymbol{r}/\hbar}$ needs to be considered as a correction due to the gauge transformation[52]. The Hartree potential $v_H(\boldsymbol{r},t)$ is defined as the Coulomb potential provided by the electron density $n(\boldsymbol{r},t)$ as

$$v_H(\boldsymbol{r},t)=\frac{e^2}{4\pi\epsilon_0}\int\mathrm{d}\boldsymbol{r}'\frac{n(\boldsymbol{r}',t)}{|\boldsymbol{r}-\boldsymbol{r}'|}, \tag{3}$$

where the electron density $n(\boldsymbol{r},t)$ is defined with the Kohn-Sham orbitals as

$$n(\boldsymbol{r},t)=\sum_j|\psi_j(\boldsymbol{r},t)|^2. \tag{4}$$

The exchange-correlation potential, $v_{xc}(\boldsymbol{r},t)$, is a functional of the electron density as well as the initial wavefunctions of both the original $|\Psi_0\rangle$ and Kohn-Sham $|\Phi_0\rangle$ systems. Thus, it can be expressed as $v_{xc}[n(\boldsymbol{r}',t'),|\Psi_0\rangle,|\Phi_0\rangle](\boldsymbol{r},t)$. In most practical applications, the initial state is chosen to be the ground state of the system. In this article, we omit the explicit dependence on the initial states, assuming that they are set to their respective ground states. Although TDDFT is a formally exact theoretical framework equivalent to the many-body Schrödinger equation, one needs to introduce approximations to $v_{xc}(\boldsymbol{r},t)$ for practical calculations. Hence, the quality and scope of the TDDFT calculations depend on the choice of the approximations. Note that the exchange-correlation vector potential $\boldsymbol{A}_{xc}(\boldsymbol{r},t)$ may be introduced in addition to the external vector potential $\boldsymbol{A}(t)$ in Eq. (2) based on the time-dependent current density functional theory[55]. However, here we simply neglect it for simplicity by setting $\boldsymbol{A}_{xc}(\boldsymbol{r},t)=0$.

When the ionic potential has spatial periodicity, one may employ Bloch's theorem and rewrite Eq. (1) as

$$i\hbar\frac{\partial}{\partial t}u_{b\boldsymbol{k}}(\boldsymbol{r},t)=\hat{h}_{\mathrm{KS},\boldsymbol{k}}(t)u_{b\boldsymbol{k}}(\boldsymbol{r},t), \tag{5}$$

where $u_{b\boldsymbol{k}}(\boldsymbol{r},t)$ is the spatially periodic part of the Bloch wavefunction, defined as $\psi_j(\boldsymbol{r},t)=e^{i\boldsymbol{k}\cdot\boldsymbol{r}}u_{b\boldsymbol{k}}(\boldsymbol{r},t)$ with the Bloch wavevector $\boldsymbol{k}$ and the band index, b. Here, the Kohn-Sham Hamiltonian is also rewritten as[52]

$$\begin{aligned}\hat{h}_{\mathrm{KS},\boldsymbol{k}}(t) &= e^{-i\boldsymbol{k}\cdot\boldsymbol{r}}\hat{h}_{\mathrm{KS}}(t)e^{i\boldsymbol{k}\cdot\boldsymbol{r}}\\ &= \tfrac{1}{2m_e}\left[\hat{\boldsymbol{p}}+\hbar\boldsymbol{k}+e\boldsymbol{A}(t)\right]^2\\ &\quad+e^{-i\left(\boldsymbol{k}+e\boldsymbol{A}(t)/\hbar\right)\cdot\boldsymbol{r}}\hat{v}_{\mathrm{ion}}e^{i\left(\boldsymbol{k}+e\boldsymbol{A}(t)/\hbar\right)\cdot\boldsymbol{r}}\\ &\quad+v_H(\boldsymbol{r},t)+v_{xc}(\boldsymbol{r},t).\end{aligned} \tag{6}$$

Note that, if the ionic potential contains spatially nonlocal parts through the pseudopotential approximation, the phase factor $e^{i\boldsymbol{k}\cdot\boldsymbol{r}}$ does not commute with the ionic potential, and it provides an additional contribution to the Kohn-Sham Hamiltonian for the periodic part of the Bloch wavefunction[52].

Transient photoelectron spectroscopy for gas systems

Methods to compute photoelectron spectrum

As a first application of TDDFT calculations to attosecond physics, we present first-principles calculations of RABBIT experiments for atomic gas systems. In the RABBIT experiments, atomic or molecular systems are irradiated with two laser pulses: one with the fundamental frequency and another provided by the high-order harmonic generation processes of the first pulse. As a result, the second pulse consists of photon energies corresponding to the odd harmonics of the first pulse. In these experiments, the photoelectrons induced by the two pulses are measured. Such experiments are used to characterize attosecond pulse trains[11] and to explore ultrafast phenomena on an extreme timescale[17,56,57].

Here, we discuss a practical and numerically efficient method to compute the photoelectron spectrum based on the time-dependent Kohn-

Sham orbitals, employing the time-dependent surface flux (t-SURFF) method[58–60]. In principle, photoelectron spectra can be evaluated by analyzing the momentum distribution of emitted electrons in vacuum regions. However, a naive implementation of such calculations requires a large computational box with a sufficiently large vacuum region to describe the dynamics of emitted electrons. To avoid such an impractically large computational box, one can rely on formal solutions of the time-dependent Schrödinger equation in vacuum regions under laser fields, called Volkov states. By employing the analytic solutions to describe the dynamics of emitted electrons in vacuum regions, the numerical calculation needs to take care of only a relatively small region around the parent ions, reducing the computational costs efficiently.

In the velocity gauge expression, where a laser field is described by a spatially-uniform vector potential, a Volkov state is given by

$$\chi_{\boldsymbol{p}}(\boldsymbol{r},t) = \sqrt{\tfrac{1}{(2\pi)^3}}\exp\left[\tfrac{i}{\hbar}(\boldsymbol{p}+e\boldsymbol{A}(t))\cdot\boldsymbol{r}\right] \times \exp\left[\tfrac{i}{\hbar}\int_{-\infty}^{t}\mathrm{d}t'\,\tfrac{1}{2m_e}(\boldsymbol{p}+e\boldsymbol{A}(t'))^2\right]. \quad (7)$$

While the electron dynamics in the vacuum region is described by Volkov states, the dynamics close to the ions can be described by the numerical solutions of the time-dependent Kohn–Sham equation[59]. This decomposition enables us to analyze the momentum-resolved photoelectron probability $\mathcal{P}(\boldsymbol{p})$ by the following flux integral through a closed surface:

$$\mathcal{P}(\boldsymbol{p}) = \frac{1}{N}\sum_j \left|\int_{-\infty}^{\infty}\mathrm{d}t\int_S \mathrm{d}\boldsymbol{s}\cdot\langle\chi_{\boldsymbol{p}}(t)|\hat{\boldsymbol{j}}|\psi_j(t)\rangle\right|^2, \quad (8)$$

where $\hat{\boldsymbol{j}}$ is the current density operator. Here, the sum over j runs over all occupied orbitals to compute the total photoelectron yield. This allows us to compute the momentum and spin-resolved photoelectron spectra. Additionally, one may limit the range of the sum to specifically investigate the photoelectron ionized from specific initial orbitals. For example, in the simulation of excited Argon gas, one can limit the sum to Argon 3p orbitals, such that the computed photoelectron probability corresponds to the yield ionized only from those orbitals. For the practical evaluation of the time integral in Eq. (8), we integrate it between the beginning, t_i, and the end, t_f, of the numerical simulations, assuming that the system remains in the ground state and there is no current flow before t_i. Additionally, we assume that the flux becomes zero after the emitted electrons move outside the closed surface.

Furthermore, by integrating over the angle of momentum, the energy-resolved photoelectron probability $\mathcal{P}(E)$ can be evaluated as

$$\mathcal{P}(E) = \int \mathrm{d}\boldsymbol{p}\mathcal{P}(\boldsymbol{p})\delta\left(\frac{\boldsymbol{p}^2}{2m}-E\right). \quad (9)$$

The schematic picture in Fig. 1 illustrates the geometry employed in practical TDDFT calculations for evaluating the photoelectron spectrum. The surface for the flux integral separates the computational region into the inner (colored in green) and outer (colored in yellow) parts. The time-dependent Kohn-Sham equations are solved in the inner part, while a complex absorption potential (CAP) is introduced in the outer part to eliminate reflected electrons from the computational box boundary[59].

Application to RABBIT measurement

Here, we introduce a first-principles simulation for the RABBIT measurement by applying the t-SURFF method with a pump-probe setup. Then, we demonstrate the RABBIT simulation results as reported in ref. 47.

To perform the RABBIT simulation, we compute electron dynamics in atomic or molecular systems under an infrared (IR) laser field and extreme ultraviolet (EUV) attosecond pulse trains. As an IR pulse, we consider the

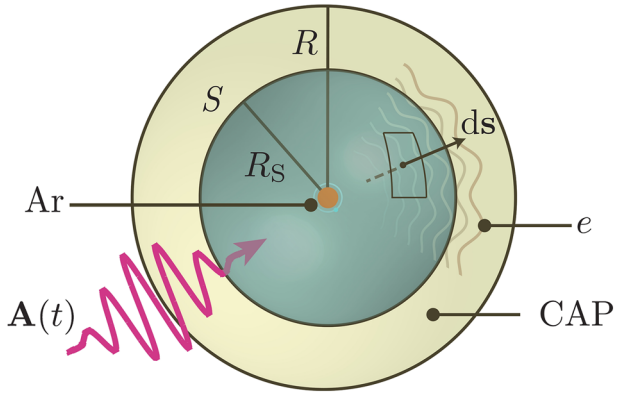

Fig. 1 | Schematic of the t-SURFF Method. Scheme illustrating the geometry employed to calculate the photoelectron spectrum with t-SURFF and TDDFT. Adapted from Ref. 47.

following form for the vector potential,

$$\boldsymbol{A}_{\mathrm{IR}}(t) = -\boldsymbol{e}_z\frac{E_{\mathrm{IR}}}{\omega_{\mathrm{IR}}}\cos^2\left(\frac{\pi t}{T_{\mathrm{IR}}}\right)\sin(\omega_{\mathrm{IR}}t) \quad (10)$$

in the domain, $-T_{\mathrm{IR}}/2 < t < T_{\mathrm{IR}}/2$, and zero outside. We set the polarization direction $\boldsymbol{e}_z$ to the z direction, the mean photon energy $\hbar\omega_{\mathrm{IR}}$ to 1.55 eV, the full pulse duration T_{IR} to 30 fs, and the peak field strength E_{IR} to 8.68 MV/cm.

Similarly, the EUV attosecond pulse train is described as

$$\boldsymbol{A}_{\mathrm{EUV}}(t) = -\boldsymbol{e}_z\frac{E_{\mathrm{EUV}}}{\omega_{\mathrm{EUV}}}\cos^4\left(\frac{\pi t}{T_{\mathrm{train}}}\right) \times\cos^6(\omega_{\mathrm{IR}}t)\sin(\omega_{\mathrm{EUV}}t) \quad (11)$$

in the domain, $-T_{\mathrm{train}}/2 < t < T_{\mathrm{train}}/2$, and zero outside. We set ω_{EUV} to $25\omega_{\mathrm{IR}}$, T_{train} to 10 fs, and E_{EUV} to 6.14 MV/cm.

For practical calculations, we employed the *Octopus* code[61]. Numerical details for the following photoelectron calculations are provided in the previous work[47]. As the exchange-correlation potential $v_{xc}(\boldsymbol{r}, t)$, we employed the adiabatic local density approximation (ALDA) with the averaged-density self-interaction correction (ADSIC)[62,63] to correct the ionization potential of atoms. If an alternative approximated functional that does not accurately reproduce the ionization potential and the electronic structure of atoms is employed, difficulties are expected in achieving a quantitative comparison with experimental results.

Figure 2a shows the spectral intensity profile of the applied EUV electric field, $|E_{\mathrm{EUV}}(\omega)|^2$, where $E_{\mathrm{EUV}}(\omega)$ is the Fourier transform of $E_{\mathrm{EUV}}(t)$. Reflecting the temporal profile of the pulse trains, the power spectrum displays a comb structure in the frequency domain. This comb structure plays an essential role in the RABBIT measurement.

In the RABBIT measurement, the photoelectron spectra are collected under the presence of both IR and EUV laser pulses. Figure 2b shows the computed spectra of photoelectrons ionized from Argon 3p orbitals. The computed spectrum by employing only the EUV pulse trains is shown as the blue-dashed line, and it displays a comb structure with the energy spacing of $2\hbar\omega_0$, reflecting the comb structure of the EUV pulse trains in Fig. 2a. In contrast, the computed spectrum by employing both EUV and IR pulses is shown as the red-solid line in Fig. 2b, and it shows additional peaks in between the original peaks due to the additional two-photon excitation paths, which are described by the schematic picture above Fig. 2b.

The RABBIT simulation is conducted by recalculating the photoelectron spectrum with a varying time delay t_{delay} between the IR and EUV pulses. Figure 2c displays the computed RABBIT trace for the

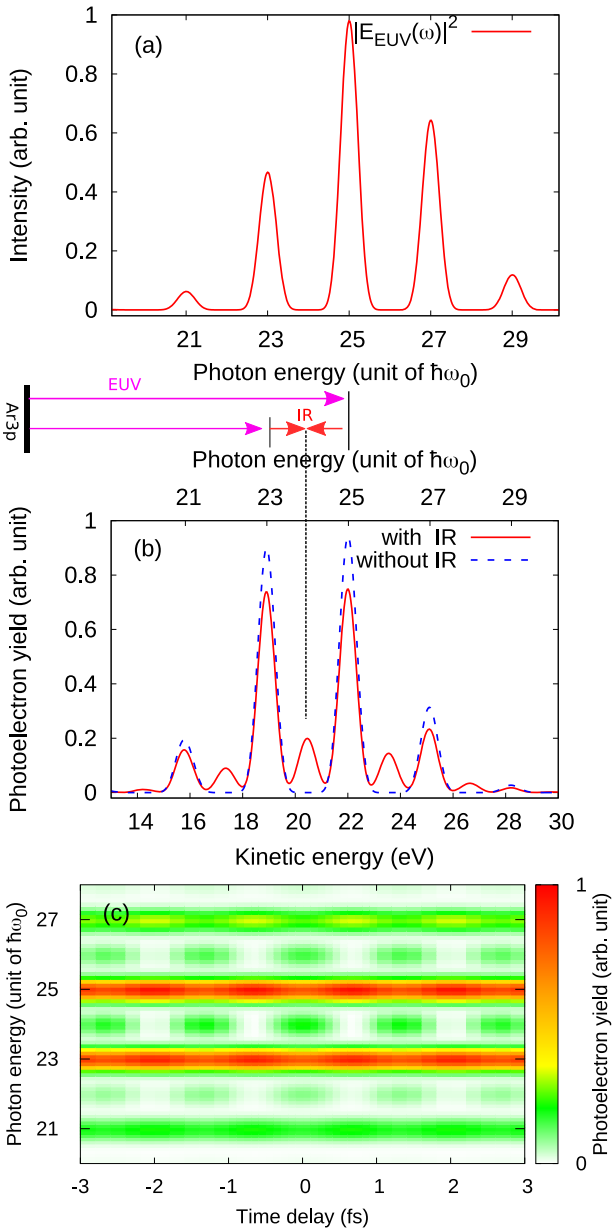

Fig. 2 | Results of the RABBIT Simulation. a The power spectrum of the applied EUV attosecond pulse trains, $|E_{\mathrm{EUV}}(\omega)|^2$, is shown. **b** The spectrum of photoelectrons ionized from Argon 3*p* orbitals computed using both IR and EUV pulses is shown as the red solid line, while that computed using solely the EUV pulse is shown as the blue dashed line. **c** The computed RABBIT trace corresponding to Argon 3*p* orbitals is shown. The schematic picture shown between **a** and **b** describes the interference of the two-photon excitation paths opened by the combination of IR and EUV pulses. Adapted from Ref. 47.

photoelectrons ionized from Argon 3*p* orbitals. As depicted in Fig. 2c, the additional peaks, induced by the two-photon excitation paths, exhibit oscillatory behavior with an oscillation period that is half of the IR field's period ($\pi/\omega_{\mathrm{IR}} \approx 1.3$ fs). The oscillation delay of these additional side peaks, relative to the time-delay between the IR and EUV pulses, contains critical information on the photoionization dynamics[56,57]. To extract this information, we initially average the RABBIT trace around the central frequency of the *n*-th sideband with a width of $\hbar\omega_0/2$ as follows:

$$S_n(t_{delay}) = \int_{n\hbar\omega_0-\frac{\hbar\omega_0}{2}}^{n\hbar\omega_0+\frac{\hbar\omega_0}{2}} \mathrm{d}E\mathcal{P}(E, t_{delay}). \tag{12}$$

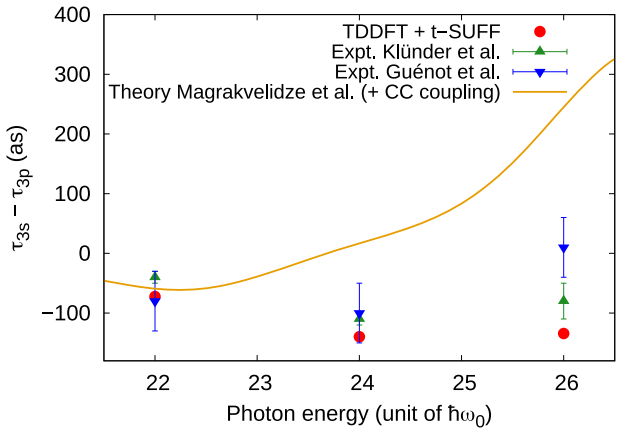

Fig. 3 | The Computed Time Delay. Comparison of the relative delay, $\tau_{3s} - \tau_{3p}$, between argon 3*s* and 3*p* orbitals. The theoretical results computed using the TDDFT + TSURFF approach are shown as red circles. The experimental results by Klünder et al., Ref. 56, are shown as green up-pointing triangles, and those by Guénot et al., Ref. 57, are shown as blue down-pointing triangles. As a reference, the theoretical results by Magrakvelidze et al., Ref. 64, are shown as the orange line. Adapted from Ref. 47.

We then fit the *n*-th order RABBIT trace, $S_n(t_{delay})$, with the function below:

$$\tilde{S}_n(t) = A\cos^4\left[\frac{\pi}{\sigma}(t_{delay} - t_0)\right]\cos^2\left[\omega_0(t_{delay} - \tau_{\mathrm{RABBIT}})\right] + C, \tag{13}$$

where *A*, *C*, σ, t_0, and τ_{RABBIT} serve as fitting parameters. In this context, τ_{RABBIT} represents the time delay between the RABBIT trace and the pump-probe delay t_{delay}.

In Fig. 2c, the RABBIT trace is investigated only for photoelectrons ionized from argon 3*p* orbitals. Therefore, by applying the above fitting analysis with Eq. (13) to the RABBIT trace in Fig. 2c, we can directly extract the RABBIT delay time for these orbitals, which we shall denote as τ_{3p}. Similarly, the RABBIT trace of photoelectrons ionized from argon 3*s* orbitals can also be investigated, and we shall denote the corresponding RABBIT delay as τ_{3s}. By calculating the difference in the extracted delay times as $\tau_{3s} - \tau_{3p}$, the difference in the photoionization delay time can be deduced.

Figure 3 shows the computed relative delays, $\tau_{3s} - \tau_{3p}$, for different side peaks. The experimental data[56,57] are also shown. By comparing the theory and experiment, the direct RABBIT simulation based on TDDFT shows good agreement with the experimental data.

The observed delay time from the RABBIT measurement is often analyzed as the sum of the Wigner-Smith delay τ_{W} and the continuum-continuum (CC) coupling delay τ_{CC}[18,57]. For example, Magrakvelidze et al. theoretically investigated the Wigner-Smith delay using TDDFT[64]. As a reference, their result is shown as the orange solid line in Fig. 3. Since Magrakvelidze et al. compared the computed Wigner-Smith delay with the experimental data by subtracting the CC coupling delay from the experimental delay, we added the CC coupling delay[57] to their Wigner-Smith delay for a consistent comparison. As seen from Fig. 3c, the ionization delay of Magrakvelidze and co-workers shows a deviation from the experimental data. In contrast, the direct RABBIT simulation with TDDFT shows a better agreement with the experiment. This discrepancy between the two theories may come from an inconsistent treatment of the different contributions. In the previous work, the Wigner-Smith delay is computed with TDDFT in the perturbative regime, while the CC coupling delay is treated differently. In contrast, the present RABBIT simulation with TDDFT simulates the whole experimental process, including ionization, propagation, and detection, on the same footing. Hence, the direct simulation of the whole RABBIT

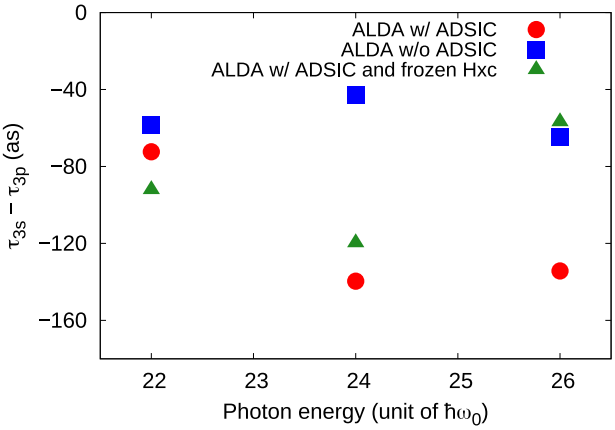

Fig. 4 | The computed time delay with different approximations. The relative delay, $\tau_{3s} - \tau_{3p}$, between the argon 3*s* and 3*p* orbitals is computed using the TDDFT + TSURFF approach with different approximations to the Hartree and exchange-correlation potentials. The results obtained with ALDA and ADSIC are represented by red circles, while those computed with ALDA but without ADSIC are shown as blue squares. The green triangles represent the results computed with ALDA and ADSIC, but with the Hartree-exchange-correlation potential frozen at the ground state.

measurement process enables us to treat all possible contributions consistently, providing an accurate description of the phenomenon.

To examine the many-body effects, we further analyze the results using different approximations for the exchange-correlation potentials. In the original TDDFT simulation, we employed ALDA and ADSIC to accurately describe the ionization potential and the local field effect, as shown in Fig. 3. In addition, we have computed results using only ALDA, without ADSIC, to elucidate the impact of errors in the electronic structure, such as the ionization potential. We also computed the ionization delay using ALDA and ADSIC while freezing the exchange-correlation potential at the ground state to clarify the role of local field effects. Figure 4 presents a comparison of the three approximations.

As shown in the figure, all approximations yield similar results at low photon energy, specifically at $22\hbar\omega_0$. However, the result obtained without ADSIC deviates from the full calculation (red circles) at higher energies (24 and $26\hbar\omega_0$), indicating that the electronic structure affects the ionization delay in this energy region. Furthermore, when the Hartree and exchange-correlation potentials are frozen at the ground state, the photoionization delay is significantly shifted from the full calculation at the highest energy ($26\hbar\omega_0$), highlighting the crucial role of local field effects at this photon energy. This result is consistent with the existence of Cooper minima and their impact on photoionization delay[18,47,65].

Transient absorption spectroscopy for solids

Static absorption of solids

After the advent of attosecond pulses, electron dynamics in atoms and molecules have been intensively investigated[66–69]. Having established an understanding of attosecond physics for isolated systems, electron dynamics in solids are now gathering much attention[13,20,48,50,70]. In this section, we discuss methods to compute static and transient optical properties of solids from first principles, following the application to attosecond transient spectroscopy for magnetic systems, specifically bulk cobalt.

We first briefly review how to compute the absorption spectra of bulk solids from first-principles calculations. Details of the method are explained elsewhere[52]. To compute the optical properties of solids, we solve the time-dependent Kohn–Sham equation for periodic systems, Eq. (5), under an impulsive distortion given by

$$\boldsymbol{A}(t) = -\boldsymbol{e}_p E_0 \Theta(t), \tag{14}$$

where $\boldsymbol{e}_p$ is a unit vector along the polarization direction of the impulsive distortion, and E_0 is its strength. The vector potential given by Eq. (14) corresponds to an impulsive electric field described by $\boldsymbol{E}(t) = -\,d\boldsymbol{A}(t)/dt = \boldsymbol{e}_p E_0 \delta(t)$.

By employing the computed Kohn–Sham orbitals, we further compute the total electric current as

$$\boldsymbol{J}(t) = -\frac{e}{m\Omega}\sum_j \int_\Omega d\boldsymbol{r}\psi_j^*(\boldsymbol{r},t)\hat{v}\psi_j(\boldsymbol{r},t), \tag{15}$$

where Ω is the volume of the unit cell defined by the periodic boundary condition, and $\hat{v}$ is the velocity operator defined as

$$\hat{v} = \frac{\left[\boldsymbol{r}, \hat{h}_{\mathrm{KS}}\right]}{i\hbar} = \frac{1}{m}\left[\hat{\boldsymbol{p}} + e\boldsymbol{A}(t)\right] + \frac{\left[\boldsymbol{r}, \hat{v}_{\mathrm{ion}}\right]}{i\hbar}. \tag{16}$$

Here, in addition to the conventional velocity operator, a nonlocal part of the pseudopotential may contribute to the velocity operator since it does not commute with the position operator.

To demonstrate the static absorption calculation for solid-state systems, we take bulk cobalt as an example, which will be used for transient absorption calculations later. In the calculations, we employ a hexagonal single-crystal structure, and we set the lattice parameter *a* to 2.51 Å and the lattice constant ratio *c*/*a* to 1.622 according to experimental data. The numerical simulations were performed with the *Octopus* code[61] by discretizing the hexagonal unit cell into $24 \times 24 \times 38$ grid points and the first Brillouin zone into 24^3*k*-points. As the exchange-correlation potential, we employ the adiabatic local spin density approximation[71].

Figure 5a shows the computed current $J(t) = \boldsymbol{e}_p \cdot \boldsymbol{J}(t)$ induced in bulk cobalt under the impulsive distortion given by Eq. (14). The inset shows the current as a function of time on a shorter timescale. As seen in the figure, the current is suddenly induced by the impulsive distortion at $t = 0$, and it exhibits oscillations with damping.

By applying the Fourier transform to the computed current under the impulsive distortion, the optical conductivity can be directly evaluated as

$$\sigma(\omega) = \frac{1}{E_0}\int_{-\infty}^{\infty} dt J(t) e^{i\omega t} e^{-\gamma t}, \tag{17}$$

where γ is a phenomenological damping constant. Furthermore, the dielectric function $\epsilon(\omega)$ and the absorption coefficient $\mu(\omega)$ can be evaluated from the optical conductivity as

$$\epsilon(\omega) = 1 + \frac{4\pi i}{\omega}\sigma(\omega), \tag{18}$$

$$\mu(\omega) = \frac{2\omega}{c}\mathrm{Im}\left[\sqrt{\epsilon(\omega)}\right]. \tag{19}$$

Figure 5b shows the computed absorption coefficient $\mu(\omega)$ from the current in Fig. 5a. As seen in the figure, the absorption coefficient of bulk cobalt shows a sharp increase in absorption around 57 eV, and this structure corresponds to the $M_{2,3}$ absorption edge.

Attosecond transient absorption of solids

First-principles simulations of attosecond transient absorption spectroscopy for solids can be viewed as an extension of the static photoabsorption calculation. Similarly to the RABBIT simulation technique presented in "Application to RABBIT measurement", one performs electron dynamics calculations in the presence of two light pulses: one is the IR pump pulse, while the other is the attosecond EUV probe pulse. This can be understood as a direct simulation of experimental attosecond pump-probe setups.

For a practical demonstration, we consider the attosecond transient absorption of bulk cobalt, employing the numerical parameters introduced in "Static absorption of solids" by using the following pump and probe light

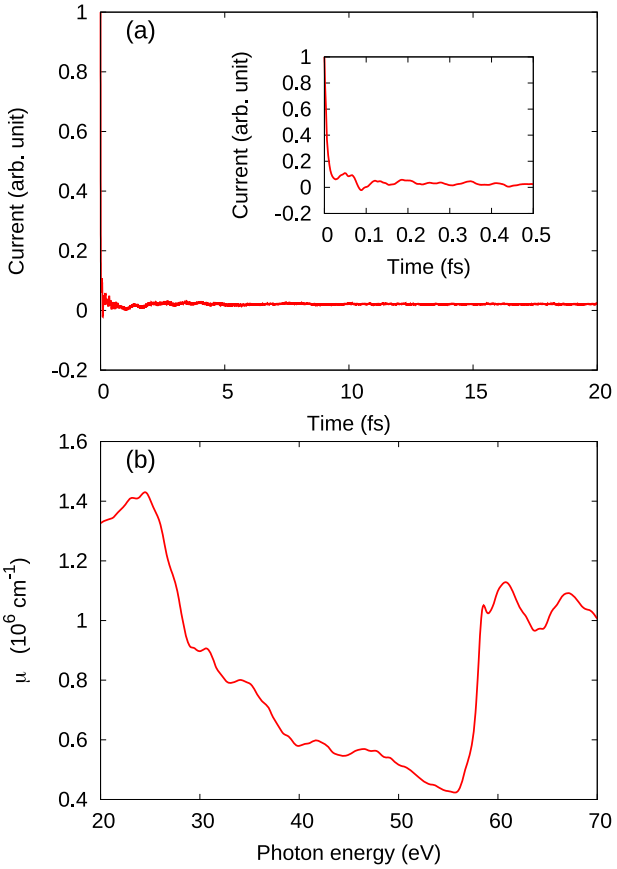

Fig. 5 | Linear Absorption of Bulk Cobalt. Linear response calculation for bulk cobalt. **a** The electric current induced by an impulsive excitation at $t = 0$ is shown as a function of time. The inset shows the current on a short timescale. **b** The computed absorption coefficient $\mu(\omega)$ of bulk cobalt is shown.

pulses:

$$\boldsymbol{A}_{\mathrm{IR}}(t) = -\frac{E_{\mathrm{IR}}}{\omega_{\mathrm{IR}}}\boldsymbol{e}_p \cos^2\left[\frac{\pi}{T_{\mathrm{IR}}}t\right]\sin(\omega_{\mathrm{IR}}t), \tag{20}$$

$$\boldsymbol{A}_{\mathrm{EUV}}(t) = -\frac{E_{\mathrm{EUV}}}{\omega_{\mathrm{EUV}}}\boldsymbol{e}_p \cos^4\left[\frac{\pi}{T_{\mathrm{EUV}}}t\right]\sin(\omega_{\mathrm{EUV}}t), \tag{21}$$

in the domain, $-T_{\mathrm{IR/EUV}}/2 < t < T_{\mathrm{IR/EUV}}/2$, and zero outside. We set E_{IR} to 8.68 MV/cm, ω_{IR} to 1.55 eV/h, T_{IR} to 20 fs, E_{EUV} to 2.75 MV/cm, ω_{EUV} to 58 eV, T_{EUV} to 1 fs, and $\boldsymbol{e}_p$ to the c-axis of the hexagonal lattice of cobalt.

To investigate the transient optical properties of solids, we perform two kinds of TDDFT simulations. One employs solely the pump pulse, $\boldsymbol{A}_{\mathrm{IR}}(t)$, and the other employs both the pump and probe pulses, $\boldsymbol{A}_{\mathrm{IR}}(t) + \boldsymbol{A}_{\mathrm{EUV}}(t - t_{\mathrm{delay}})$, with the delay time t_{delay}. We shall call the simulations of the first kind *pump-only simulations*, while those of the second kind are called *pump-probe simulations*. Furthermore, we refer to the current computed with the pump-only simulation as the pump-only current $\boldsymbol{J}^{\text{pump-only}}(t)$, and that computed with the pump-probe simulation as the pump-probe current $\boldsymbol{J}^{\text{pump-probe}}(t, t_{\mathrm{delay}})$. Note that the pump-probe current depends on the delay time t_{delay}. We further define the probe current, which is induced by the probe pulse in the presence of the pump pulse, as $\boldsymbol{J}^{\text{probe}}(t) = \boldsymbol{J}^{\text{pump-probe}}(t) - \boldsymbol{J}^{\text{pump-only}}(t)$. Importantly, the probe current contains information on the optical properties of matter in the presence of the pump pulse. Hence, the *transient* optical conductivity can be evaluated as[72]

$$\sigma^T(\omega, t_{\mathrm{delay}}) = \frac{\int_{-\infty}^{\infty} \mathrm{d}t e^{i\omega t - \gamma t}\boldsymbol{J}^{\text{probe}}(t, t_{\mathrm{delay}})\cdot\boldsymbol{e}_p}{\int_{-\infty}^{\infty} \mathrm{d}t e^{i\omega t - \gamma t}\boldsymbol{E}_{\mathrm{EUV}}(t)\cdot\boldsymbol{e}_p}. \tag{22}$$

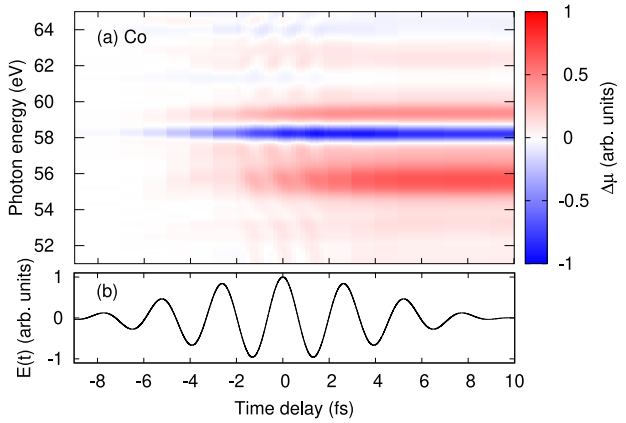

Fig. 6 | Transient Absorption of Bulk Cobalt. a The computed transient absorption spectra, $\Delta\mu^T(\omega, t_{\mathrm{delay}})$, of bulk cobalt. **b** The time profile of the IR pulse (pump pulse) is shown.

Furthermore, the transient dielectric function and absorption coefficient are evaluated as

$$\epsilon^T(\omega, t_{\mathrm{delay}}) = 1 + \frac{4\pi i}{\omega}\sigma^T(\omega, t_{\mathrm{delay}}), \tag{23}$$

$$\mu^T(\omega, t_{\mathrm{delay}}) = \frac{2\omega}{c}\mathrm{Im}\left[\sqrt{\epsilon^T(\omega, t_{\mathrm{delay}})}\right]. \tag{24}$$

The first-principles calculation of these transient optical properties is a powerful tool to analyze recent attosecond experiments and provides microscopic insight into the experimental results[20–22,51].

Figure 6a shows the computed transient absorption spectra, $\Delta\mu^T(\omega, t_{\mathrm{delay}}) = \mu^T(\omega, t_{\mathrm{delay}}) - \mu(\omega)$. As a reference, the time profile of the pump pulse is shown in Fig. 6b. As seen from the figures, the absorption of bulk cobalt sharply decreases around the energy of 58 eV, where the $M_{2,3}$ absorption edge is located, due to the pump laser irradiation, and the reduction in absorption persists even after the laser irradiation. The sharp reduction in photoabsorption around the edge of bulk cobalt has been investigated with the finite electron temperature TDDFT simulation in Ref. 73, assuming that the electronic system is quasi-thermalized after the laser irradiation. In contrast, the pump-probe simulation here demonstrates that such a sharp reduction in photoabsorption occurs even in the nonequilibrium phase before electron thermalization.

In addition to the sharp reduction in photoabsorption around the absorption edge, an increase in photoabsorption in a wider photon energy range is also observed in Fig. 6a. Such an increase in photoabsorption around the absorption edge has been observed in the transient responses of transition metals and has been understood by light-induced electron localization and the modification of the screening effect[22,51,52].

To demonstrate the utility of the computational technique, we compute the electron density distribution after the laser irradiation ($t = 10$ fs) to obtain further insight into the transient absorption of bulk cobalt. Figure 7a shows the total electron density in the ground state. Here, a cobalt atom is located at the origin (0, 0). Figure 7b and c show the change in the electron density distribution due to the laser irradiation for (b) majority-spin and (c) minority-spin electrons. Since we intentionally did not include spin-orbit coupling in the present simulations, the population of each spin of electrons is conserved under laser irradiation. Therefore, Fig. 7b shows that the majority-spin electrons are expelled from the region close to the atoms by the laser irradiation, while Fig. 7c indicates that the minority-spin electrons are gathering around the atomic region. As a result, the spin polarization at the atomic site decreases due to the laser irradiation.

In Ref. 73, finite electron-temperature simulations for a hot-electron state also show a reduction in local spin polarization with an increase in

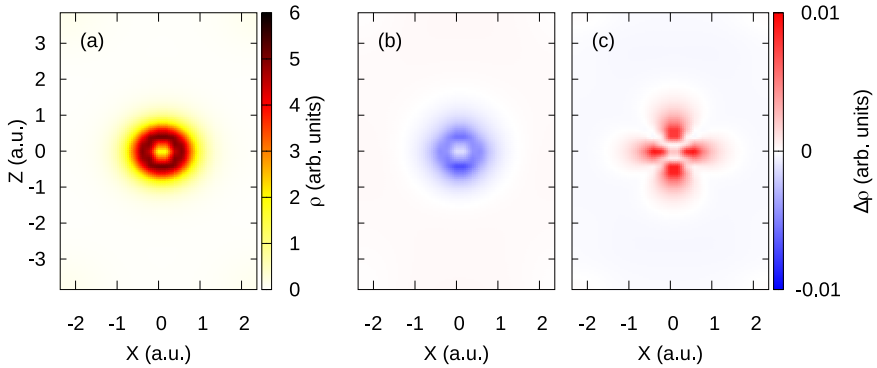

Fig. 7 | Electron and Spin Density in Bulk Cobalt. The electron density in bulk cobalt, with the cobalt atom located at the origin in each panel. **a** The total electron density in the ground state. **b** The change in the density of majority spin electrons after laser irradiation. **c** The change in the density of minority spin electrons after laser irradiation.

electron temperature. Furthermore, the reduction in local spin polarization further reduces the exchange-splitting of cobalt 3*p* states, and the absorption edge is blue-shifted, resulting in a sharp reduction of transient absorption. However, in previous work, the origin of the local spin polarization was unclear because both spin-flipping and spatial spin-transport processes are allowed in the thermal calculations. In the present pump-probe calculations, the spin-flipping process is forbidden by omitting the spin-orbit coupling. Nevertheless, the reduction of local spin polarization is observed even in the present pump-probe calculations. Therefore, the reduction of local spin polarization is expected to originate from the spatial spin transfer, where majority-spin electrons are expelled from the atomic site and minority-spin electrons are localized at the atomic site by the laser driving.

Solid-state high-order harmonic generation and nonlinear optics

Following the observation of HHG in ZnO[74], solid-state HHG has garnered significant interest from both fundamental and technological perspectives[75], as it offers novel opportunities to explore highly nonlinear light-induced electron dynamics in matter and to provide a potential for developing novel light sources beyond attosecond pulse generation with gas-phase HHG. However, solid-state HHG relies on the complex electron dynamics in solids in nonperturbatively nonlinear regimes, and its microscopic mechanism remains to be clarified. The first-principles electron dynamics calculations based on TDDFT are also useful for investigating such highly complex nonlinear phenomena, and they have been applied to solid-state HHG[76–83]. In this section, we briefly present numerical methods for evaluating HHG in solids with TDDFT.

For the evaluation of the HHG spectra, we first compute the electric current $\boldsymbol{J}(t)$ induced by a pulsed electric field $\boldsymbol{E}(t)$ with Eq. (15). The power spectrum $I_{\mathrm{HHG}}(\omega)$ of the emitted photons by HHG can be evaluated with the Fourier transform of the current as

$$I_{\mathrm{HHG}}(\omega) = \omega^2 \left| \int_{-\infty}^{\infty} \mathrm{d}t W(t) \boldsymbol{J}(t) e^{i\omega t} \right|^2, \tag{25}$$

where $W(t)$ is a window function introduced to reduce the numerical noise due to finite simulation time. We note that Eq.(25) is a commonly used approach to theoretically investigate HHG. However, the macroscopic propagation effects of light are not taken into account in this approach. To investigate such propagation effects, one may combine TDDFT with the macroscopic Maxwell equation to consistently describe light-induced electron dynamics and the propagation of light[43,78].

To demonstrate the first-principles calculations for solid-state HHG, we compute the electron dynamics in crystalline silicon. As an applied electric field, we use the vector potential given by Eq. (20) but with different laser parameters. Here, we set ω_{IR} to 0.413 eV, T_{IR} 25 fs, and $\boldsymbol{e}_p$ to align with the (001)-axis of the unit cell of silicon. We compute electron dynamics for different laser field strengths E_0.

Figure 8a shows the computed current as a function of time for different electric field strengths E_0. The currents are scaled with E_0 for

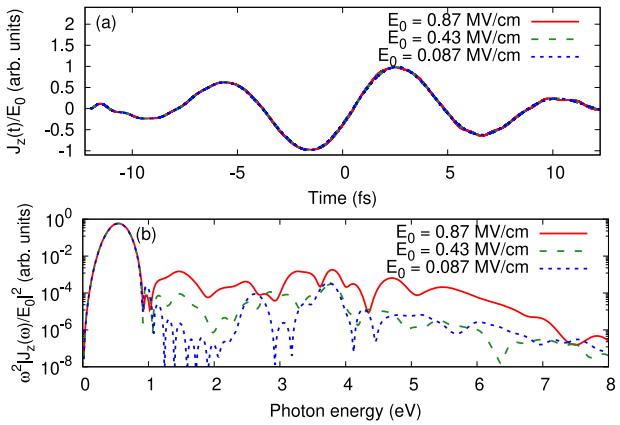

Fig. 8 | High-Order Harmonic Generation from Bulk Silicon. a The electric current in crystalline silicon induced by a laser pulse. **b** The computed HHG spectrum obtained by applying the Fourier transform to the current in **a**.

comparison. As seen from Fig. 8a, the scaled currents are very similar to each other, indicating that the induced currents are predominantly determined by the linear response.

We then analyze the HHG spectra with Eq. (25) by applying the Fourier transform to the currents in Fig. 8a. As a window function, $W(t)$, in Eq. (25), we use the envelope function of the laser pulse. Figure 8b shows the computed HHG spectra. The results are scaled by E_0^2 for comparison. As seen from Fig. 8b, there is a prominent peak at 0.41 eV, which corresponds to the photon energy of the laser pulse. For different field strengths E_0, the first peaks are almost identical to each other, indicating that the peak at the fundamental frequency is dominated by the linear response. In the higher energy region, the emitted photon spectra exhibit deviations among different field strengths, indicating that higher-energy photon emissions originate from nonlinear optical effects. Furthermore, the irradiation of higher field strength lasers leads to stronger emission of high-energy photons. We note that the spectra in Fig. 8 do not exhibit a clear peak structure, except for the fundamental peak at 0.41 eV, whereas distinct peaks are observed in the experimental results. The absence of a peak structure in the quantum dynamics calculations arises from an overly coherent channel due to the lack of proper decoherence mechanisms[84,85] and macroscopic effects[78]. Therefore, once these effects are incorporated phenomenologically or from first principles, the peak structures can be recovered.

Here, we computed the HHG spectra of silicon by fixing the polarization angle. However, one can further investigate the polarization angle dependence of HHG by manipulating the relative angle between the light polarization and crystal angle. Such analysis can provide insight into the microscopic process of HHG and has been investigated from both theoretical and experimental perspectives[86–88].

In the above analysis, HHG was investigated with TDDFT by analyzing the current $\boldsymbol{J}(t)$ induced by electric fields $\boldsymbol{E}(t)$. Since TDDFT provides $\boldsymbol{J}(t)$ as

an output by using $\boldsymbol{E}(t)$ as an input, it can be seen as a machinery for computing $\boldsymbol{J}(t)$ as a functional of $\boldsymbol{E}(t')$: $\boldsymbol{J}[\boldsymbol{E}(t')](t)$. This feature enables the computation of linear and nonlinear optical properties of materials based on TDDFT. For example, the induced current $\boldsymbol{J}(t)$ can be expanded by electric fields as

$$\begin{aligned} J_\alpha(t) &= \sum_\beta \int_{-\infty}^{\infty} \sigma_{\alpha\beta}(t-t')\mathrm{d}t' E_\beta(t') \\ &+ \sum_{\beta\gamma} \int_{-\infty}^{\infty} \mathrm{d}t' \int_{-\infty}^{\infty} \mathrm{d}t'' \sigma^{(2)}_{\alpha\beta\gamma}(t-t', t-t'') E_\beta(t') E_\gamma(t') \\ &+ \cdots, \end{aligned} \tag{26}$$

where $J_\alpha(t)$ and $E_\alpha(t)$ are α-components of $\boldsymbol{J}(t)$ and $\boldsymbol{E}(t)$. The linear and second-order nonlinear conductivity tensors are introduced as $\sigma_{\alpha\beta}(t-t')$ and $\sigma^{(2)}_{\alpha\beta\gamma}(t-t', t-t'')$. By introducing the polarization as a time-integral of the current as $\left(\boldsymbol{P}(t) = \int_{-\infty}^{t} \mathrm{d}t' \boldsymbol{J}(t')\right)$, a similar expression for the polarization and optical susceptibilities can be obtained as follows:

$$\begin{aligned} P_\alpha(t) &= \sum_\beta \int_{-\infty}^{\infty} \mathrm{d}t' \chi_{\alpha\beta}(t-t') E_\beta(t') \\ &+ \sum_{\beta\gamma} \int_{-\infty}^{\infty} \mathrm{d}t' \int_{-\infty}^{\infty} \mathrm{d}t'' \chi^{(2)}_{\alpha\beta\gamma}(t-t', t-t'') E_\beta(t') E_\gamma(t'') \\ &+ \cdots, \end{aligned} \tag{27}$$

where $\chi_{\alpha\beta}(t-t')$ and $\chi^{(2)}_{\alpha\beta\gamma}(t-t', t-t'')$ are linear and nonlinear susceptibilities. Based on these expressions, one can investigate linear and nonlinear optical properties of materials by analyzing the computed current $\boldsymbol{J}(t)$ and the corresponding driving field $\boldsymbol{E}(t)$. For example, the calculation of the static absorption of solids in "Static absorption of solids" is a primary example of such analysis. Furthermore, the extraction of nonlinear optical constants from the nonlinear electron dynamics with TDDFT has been demonstrated[89,90]. Beyond the linear and relatively lower-order nonlinear optical responses, real-time electron dynamics simulations are also applicable to nonperturbatively nonlinear phenomena, as they rely on the direct numerical integration of the time-dependent Kohn-Sham equation in the time domain without any perturbative expansion.

Conclusions and perspective

In this review, we discuss the applications of first-principles electron dynamics calculations based on TDDFT in attosecond physics to investigate ultrafast electron dynamics in both gas-phase atoms and solid-state materials. We have shown that these simulations provide macroscopic quantities directly comparable to the corresponding experiments and enable the extraction of relevant microscopic information about the mechanism driving the nonlinear electron dynamics in matter. We first introduce the basic theory of TDDFT for describing electron dynamics in matter in the presence of light fields, and then we proceed to each application.

We reviewed the first-principles calculations for photoelectron spectroscopy in gas systems by combining TDDFT calculations and the t-SURFF method. We then extend the photoelectron spectrum analysis with the pump-probe setup to examine the RABBIT measurement, demonstrating that the TDDFT simulation of the whole experimental process, involving ionization, propagation, and detection in the presence of both pump and probe pulses, is key to providing theoretical results that are comparable with experimental data.

Furthermore, we review the first-principles calculations of optical properties of solids. We start with a linear response calculation in the time domain to obtain absorption spectra of solids in the equilibrium phase. We then extend this calculation by including two light pulses: one is a pump pulse, and the other is a probe pulse, constituting the pump-probe setup. The TDDFT pump-probe simulation allows us to investigate the transient optical properties of matter in the nonequilibrium phase. We applied it to the attosecond transient absorption spectroscopy for bulk cobalt. As a result, we observed a sharp reduction in the photoabsorption around the $M_{2,3}$ absorption edge of cobalt. To unveil the microscopic mechanism behind this observation, we further analyzed the electron density dynamics driven by the pump pulse. We found that majority-spin electrons are expelled from the atomic region by the laser excitation, while minority-spin electrons gather around the atomic region. Consequently, the local spin polarization at the atomic site is reduced by the laser excitation. Furthermore, the reduction of the local spin polarization decreases the exchange splitting of the core states and causes the blue shift of the absorption edge, resulting in the sharp reduction of absorption around the edge. This observation indicates that the absorption spectrum around the absorption edge of magnetic systems is sensitive to the local magnetic properties, and thus, the local spin dynamics can be investigated via the transient absorption spectroscopy with attosecond time resolution in an element-specific manner.

We also demonstrate that TDDFT simulation can be used to analyze HHG from solids by analyzing the current induced by an intense laser pulse. Since the real-time electron dynamics simulation does not rely on any perturbative expansion but directly solves the time-dependent Kohn-Sham equation, it is applicable to nonperturbatively nonlinear optical phenomena such as HHG. Furthermore, we discuss the applicability of TDDFT simulations for investigating linear and relatively low-order nonlinear optical effects by considering TDDFT simulations as a machinery to practically compute the current $\boldsymbol{J}[\boldsymbol{E}(t')](t)$ or polarization $\boldsymbol{P}[\boldsymbol{E}(t')](t)$ as a functional of the applied fields. This viewpoint enables us to analyze various optical properties of materials from first principles.

Although TDDFT is an exact theoretical framework[39] and has been demonstrated to provide valuable insights into ultrafast phenomena[20–22,40–52], practical calculations necessitate several approximations. A primary approximation involves the exchange-correlation potential and functional. For practical applications, approximations of local or semi-local quantities, such as the local density approximation (LDA), the generalized gradient approximation (GGA), and meta-GGA, are utilized. However, these approximations accurately describe only relatively weakly correlated systems and dynamics. Furthermore, in most practical applications, the adiabatic approximation for the exchange-correlation potential is employed by neglecting the dependence of the density at past times ($t' < t$), $n(\boldsymbol{r}, t')$, resulting in $v_{xc}[n(\boldsymbol{r}', t')](\boldsymbol{r}, t) \approx v_{xc}[n(\boldsymbol{r}', t)](\boldsymbol{r}, t)$. Since the memory effect is expected to have only a minor contribution when a mean-field picture works well for the phenomena of interest, the adiabatic approximation effectively explains experimental observations. However, when the mean-field picture breaks down, the memory effect may become significant. For instance, when relaxation and decoherence due to electron-electron scattering becomes substantial, it may be necessary to include nonadiabaticity in the description[91–93]. The improvement and inclusion of memory effects are significantly linked to the development of the exchange-correlation vector potential beyond the scalar exchange-correlation potentials[94,95]. Significant advancements in the approximation of the density functional are required to depict light-induced ultrafast phenomena in correlated systems effectively[96–103].

Additionally, approximations are commonly used to describe electron-ion interactions. In most applications concerning ultrafast phenomena on the attosecond timescale, the ionic systems are considered completely frozen, neglecting their dynamics. Nonetheless, ion dynamics play a crucial role in explaining the decoherence and relaxation of excited electrons. Currently, the semi-classical treatment of electron-ion interaction, based on Ehrenfest dynamics, represents the state-of-the-art for practical calculations[104]. For a precise description of decoherence and relaxation, however, incorporating the quantum nature of ions and phonons is essential. Another aspect needing improvement is the pseudopotential approximation. In most applications, core electrons are frozen under this approximation, focusing only on valence electron dynamics. Yet, the energy spectrum of current attosecond laser pulses extends to the binding energy of core levels, necessitating an efficient numerical implementation of core electron dynamics to explore attosecond experiments thoroughly. The further development of the theoretical and numerical methods combined with advances in laser technology will open a path to explore light-induced nonequilibrium and nonlinear phenomena and a novel way to control material properties and functionalities on an ultrafast timescale.

Data availability

The code used for the research is available at https://gitlab.com/octopus-code.

Received: 5 November 2024; Accepted: 21 June 2025;
Published online: 15 July 2025

References

1. Schawlow, A. L. & Townes, C. H. Infrared and optical masers. *Phys. Rev.* **112**, 1940–1949 (1958).
2. Franken, P. A., Hill, A. E., Peters, C. W. & Weinreich, G. Generation of optical harmonics. *Phys. Rev. Lett.* **7**, 118–119 (1961).
3. Mourou, G. et al. Exawatt-zettawatt pulse generation and applications. *Opt. Commun.* **285**, 720–724 (2012).
4. Brabec, T. & Krausz, F. Intense few-cycle laser fields: Frontiers of nonlinear optics. *Rev. Mod. Phys.* **72**, 545–591 (2000).
5. Strickland, D. & Mourou, G. Compression of amplified chirped optical pulses. *Opt. Commun.* **56**, 219–221 (1985).
6. McPherson, A. et al. Studies of multiphoton production of vacuum-ultraviolet radiation in the rare gases. *J. Opt. Soc. Am. B* **4**, 595–601 (1987).
7. Ferray, M. et al. Multiple-harmonic conversion of 1064 nm radiation in rare gases. *J. Phys. B: At. Mol. Opt. Phys.* **21**, L31 (1988).
8. Corkum, P. B. Plasma perspective on strong field multiphoton ionization. *Phys. Rev. Lett.* **71**, 1994–1997 (1993).
9. Lewenstein, M., Balcou, P., Ivanov, M. Y., L'Huillier, A. & Corkum, P. B. Theory of high-harmonic generation by low-frequency laser fields. *Phys. Rev. A* **49**, 2117–2132 (1994).
10. Krausz, F. & Ivanov, M. Attosecond physics. *Rev. Mod. Phys.* **81**, 163–234 (2009).
11. Paul, P. M. et al. Observation of a train of attosecond pulses from high harmonic generation. *Science* **292**, 1689–1692 (2001).
12. Hentschel, M. et al. Attosecond metrology. *Nature* **414**, 509–513 (2001).
13. Borrego-Varillas, R., Lucchini, M. & Nisoli, M. Attosecond spectroscopy for the investigation of ultrafast dynamics in atomic, molecular and solid-state physics. *Rep. Prog. Phys.* **85**, 066401 (2022).
14. Calegari, F. & Martin, F. Open questions in attochemistry. *Commun. Chem.* **6**, 184 (2023).
15. Eckle, P. et al. Attosecond ionization and tunneling delay time measurements in helium. *Science* **322**, 1525–1529 (2008).
16. Schultze, M. et al. Delay in photoemission. *Science* **328**, 1658–1662 (2010).
17. Isinger, M. et al. Photoionization in the time and frequency domain. *Science* **358**, 893–896 (2017).
18. Pazourek, R., Nagele, S. & Burgdörfer, J. Attosecond chronoscopy of photoemission. *Rev. Mod. Phys.* **87**, 765–802 (2015).
19. Sommer, A. et al. Attosecond nonlinear polarization and light–matter energy transfer in solids. *Nature* **534**, 86–90 (2016).
20. Lucchini, M. et al. Attosecond dynamical Franz-Keldysh effect in polycrystalline diamond. *Science* **353**, 916–919 (2016).
21. Buades, B. et al. Attosecond state-resolved carrier motion in quantum materials probed by soft x-ray XANES. *Appl. Phys. Rev.* **8**, 011408 (2021).
22. Volkov, M. et al. Attosecond screening dynamics mediated by electron localization in transition metals. *Nat. Phys.* **15**, 1145–1149 (2019).
23. Lucchini, M. et al. Unravelling the intertwined atomic and bulk nature of localised excitons by attosecond spectroscopy. *Nat. Commun.* **12**, 1021 (2021).
24. Géneaux, R. et al. Attosecond time-domain measurement of core-level-exciton decay in magnesium oxide. *Phys. Rev. Lett.* **124**, 207401 (2020).
25. Zuo, T., Bandrauk, A. & Corkum, P. Laser-induced electron diffraction: a new tool for probing ultrafast molecular dynamics. *Chem. Phys. Lett.* **259**, 313–320 (1996).
26. Lein, M., Marangos, J. P. & Knight, P. L. Electron diffraction in above-threshold ionization of molecules. *Phys. Rev. A* **66**, 051404 (2002).
27. Lin, C. D., Le, A.-T., Chen, Z., Morishita, T. & Lucchese, R. Strong-field rescattering physics—self-imaging of a molecule by its own electrons. *J. Phys. B: At. Mol. Opt. Phys.* **43**, 122001 (2010).
28. Pullen, M. G. et al. Imaging an aligned polyatomic molecule with laser-induced electron diffraction. *Nat. Commun.* **6**, 7262 (2015).
29. Lundh, O. et al. Few femtosecond, few kiloampere electron bunch produced by a laser–plasma accelerator. *Nat. Phys.* **7**, 219–222 (2011).
30. Priebe, K. E. et al. Attosecond electron pulse trains and quantum state reconstruction in ultrafast transmission electron microscopy. *Nat. Photonics* **11**, 793–797 (2017).
31. Morimoto, Y. & Baum, P. Diffraction and microscopy with attosecond electron pulse trains. *Nat. Phys.* **14**, 252–256 (2018).
32. Morimoto, Y. & Baum, P. Single-cycle optical control of beam electrons. *Phys. Rev. Lett.* **125**, 193202 (2020).
33. Schiffrin, A. et al. Optical-field-induced current in dielectrics. *Nature* **493**, 70–74 (2013).
34. Krausz, F. & Stockman, M. I. Attosecond metrology: from electron capture to future signal processing. *Nat. Photonics* **8**, 205–213 (2014).
35. Higuchi, T., Heide, C., Ullmann, K., Weber, H. B. & Hommelhoff, P. Light-field-driven currents in graphene. *Nature* **550**, 224–228 (2017).
36. Lee, J. D., Yun, W. S. & Park, N. Rectifying the optical-field-induced current in dielectrics: Petahertz diode. *Phys. Rev. Lett.* **116**, 057401 (2016).
37. Schoetz, J. et al. Perspective on petahertz electronics and attosecond nanoscopy. *ACS Photonics* **6**, 3057–3069 (2019).
38. Boolakee, T. et al. Light-field control of real and virtual charge carriers. *Nature* **605**, 251–255 (2022).
39. Runge, E. & Gross, E. K. U. Density-functional theory for time-dependent systems. *Phys. Rev. Lett.* **52**, 997–1000 (1984).
40. Yabana, K. & Bertsch, G. F. Time-dependent local-density approximation in real time. *Phys. Rev. B* **54**, 4484–4487 (1996).
41. Bertsch, G. F., Iwata, J.-I., Rubio, A. & Yabana, K. Real-space, real-time method for the dielectric function. *Phys. Rev. B* **62**, 7998–8002 (2000).
42. Otobe, T. et al. First-principles electron dynamics simulation for optical breakdown of dielectrics under an intense laser field. *Phys. Rev. B* **77**, 165104 (2008).
43. Yabana, K., Sugiyama, T., Shinohara, Y., Otobe, T. & Bertsch, G. F. Time-dependent density functional theory for strong electromagnetic fields in crystalline solids. *Phys. Rev. B* **85**, 045134 (2012).
44. Sato, S. A. et al. Time-dependent density functional theory of high-intensity short-pulse laser irradiation on insulators. *Phys. Rev. B* **92**, 205413 (2015).
45. Andrea Rozzi, C. et al. Quantum coherence controls the charge separation in a prototypical artificial light-harvesting system. *Nat. Commun.* **4**, 1602 (2013).
46. Castro, A., Marques, M. A. L., Alonso, J. A., Bertsch, G. F. & Rubio, A. Excited states dynamics in time-dependent density functional theory. *Eur. Phys. J. D. - At. Mol., Opt. Plasma Phys.* **28**, 211–218 (2004).
47. Sato, S. A., Hübener, H., Rubio, A. & De Giovannini, U. First-principles simulations for attosecond photoelectron spectroscopy based on time-dependent density functional theory. *Eur. Phys. J. B* **91**, 126 (2018).
48. Schultze, M. et al. Attosecond band-gap dynamics in silicon. *Science* **346**, 1348–1352 (2014).
49. Zürch, M. et al. Direct and simultaneous observation of ultrafast electron and hole dynamics in germanium. *Nat. Commun.* **8**, 15734 (2017).
50. Siegrist, F. et al. Light-wave dynamic control of magnetism. *Nature* **571**, 240–244 (2019).

51. Schumacher, Z. et al. Ultrafast electron localization and screening in a transition metal dichalcogenide. *Proc. Natl Acad. Sci.* **120**, e2221725120 (2023).
52. Sato, S. A. First-principles calculations for attosecond electron dynamics in solids. *Comput. Mater. Sci.* **194**, 110274 (2021).
53. Kleinman, L. & Bylander, D. M. Efficacious form for model pseudopotentials. *Phys. Rev. Lett.* **48**, 1425–1428 (1982).
54. Troullier, N. & Martins, J. L. Efficient pseudopotentials for plane-wave calculations. *Phys. Rev. B* **43**, 1993–2006 (1991).
55. Vignale, G. Mapping from current densities to vector potentials in time-dependent current density functional theory. *Phys. Rev. B* **70**, 201102 (2004).
56. Klünder, K. et al. Probing single-photon ionization on the attosecond time scale. *Phys. Rev. Lett.* **106**, 143002 (2011).
57. Guénot, D. et al. Photoemission-time-delay measurements and calculations close to the 3s-ionization-cross-section minimum in Ar. *Phys. Rev. A* **85**, 053424 (2012).
58. Tao, L. & Scrinzi, A. Photo-electron momentum spectra from minimal volumes: the time-dependent surface flux method. *N. J. Phys.* **14**, 013021 (2012).
59. Wopperer, P., De Giovannini, U. & Rubio, A. Efficient and accurate modeling of electron photoemission in nanostructures with TDDFT. *Eur. Phys. J. B* **90**, 51 (2017).
60. de Giovannini, U., Hübener, H. & Rubio, A. A first-principles time-dependent density functional theory framework for spin and time-resolved angular-resolved photoelectron spectroscopy in periodic systems. *J. Chem. Theory Comput.* **13**, 265–273 (2017).
61. Tancogne-Dejean, N. et al. Octopus, a computational framework for exploring light-driven phenomena and quantum dynamics in extended and finite systems. *J. Chem. Phys.* **152**, 124119 (2020).
62. Perdew, J. P. & Zunger, A. Self-interaction correction to density-functional approximations for many-electron systems. *Phys. Rev. B* **23**, 5048–5079 (1981).
63. Legrand, C., Suraud, E. & Reinhard, P.-G. Comparison of self-interaction-corrections for metal clusters. *J. Phys. B: At. Mol. Opt. Phys.* **35**, 1115 (2002).
64. Magrakvelidze, M., Madjet, M. E.-A., Dixit, G., Ivanov, M. & Chakraborty, H. S. Attosecond time delay in valence photoionization and photorecombination of argon: A time-dependent local-density-approximation study. *Phys. Rev. A* **91**, 063415 (2015).
65. Möbus, B. et al. Measurements of absolute Ar 3s photoionization cross sections. *Phys. Rev. A* **47**, 3888–3893 (1993).
66. Goulielmakis, E. et al. Real-time observation of valence electron motion. *Nature* **466**, 739–743 (2010).
67. Wang, H. et al. Attosecond time-resolved autoionization of argon. *Phys. Rev. Lett.* **105**, 143002 (2010).
68. Holler, M., Schapper, F., Gallmann, L. & Keller, U. Attosecond electron wave-packet interference observed by transient absorption. *Phys. Rev. Lett.* **106**, 123601 (2011).
69. Reduzzi, M. et al. Observation of autoionization dynamics and sub-cycle quantum beating in electronic molecular wave packets. *J. Phys. B: At. Mol. Opt. Phys.* **49**, 065102 (2016).
70. Mashiko, H., Oguri, K., Yamaguchi, T., Suda, A. & Gotoh, H. Petahertz optical drive with wide-bandgap semiconductor. *Nat. Phys.* **12**, 741–745 (2016).
71. Perdew, J. P. & Wang, Y. Accurate and simple analytic representation of the electron-gas correlation energy. *Phys. Rev. B* **45**, 13244–13249 (1992).
72. Sato, S. A., Yabana, K., Shinohara, Y., Otobe, T. & Bertsch, G. F. Numerical pump-probe experiments of laser-excited silicon in nonequilibrium phase. *Phys. Rev. B* **89**, 064304 (2014).
73. Sato, S. A. First-principles calculations for transient absorption of laser-excited magnetic materials. *Electron. Struct.* **4**, 014007 (2022).
74. Ghimire, S. et al. Observation of high-order harmonic generation in a bulk crystal. *Nat. Phys.* **7**, 138–141 (2011).
75. Ghimire, S. & Reis, D. A. High-harmonic generation from solids. *Nat. Phys.* **15**, 10–16 (2019).
76. Otobe, T. First-principle description for the high-harmonic generation in a diamond by intense short laser pulse. *J. Appl. Phys.* **111**, 093112 (2012).
77. Tancogne-Dejean, N., Mücke, O. D., Kärtner, F. X. & Rubio, A. Impact of the electronic band structure in high-harmonic generation spectra of solids. *Phys. Rev. Lett.* **118**, 087403 (2017).
78. Floss, I. et al. Ab initio multiscale simulation of high-order harmonic generation in solids. *Phys. Rev. A* **97**, 011401 (2018).
79. Guan, M., Hu, S., Zhao, H., Lian, C. & Meng, S. Toward attosecond control of electron dynamics in two-dimensional materials. *Appl. Phys. Lett.* **116**, 043101 (2020).
80. Hu, S.-Q., Chen, D.-Q., Du, L.-L. & Meng, S. Solid-state high harmonic spectroscopy for all-optical band structure probing of high-pressure quantum states. *Proc. Natl Acad. Sci.* **121**, e2316775121 (2024).
81. Lakhotia, H. et al. Laser picoscopy of valence electrons in solids. *Nature* **583**, 55–59 (2020).
82. Hansen, K. K., Deffge, T. & Bauer, D. High-order harmonic generation in solid slabs beyond the single-active-electron approximation. *Phys. Rev. A* **96**, 053418 (2017).
83. Bauer, D. & Hansen, K. K. High-harmonic generation in solids with and without topological edge states. *Phys. Rev. Lett.* **120**, 177401 (2018).
84. Vampa, G. et al. Theoretical analysis of high-harmonic generation in solids. *Phys. Rev. Lett.* **113**, 073901 (2014).
85. Freeman, D., Kheifets, A., Yamada, S., Yamada, A. & Yabana, K. High-order harmonic generation in semiconductors driven at near- and mid-infrared wavelengths. *Phys. Rev. B* **106**, 075202 (2022).
86. Liu, H. et al. High-harmonic generation from an atomically thin semiconductor. *Nat. Phys.* **13**, 262–265 (2017).
87. Kaneshima, K. et al. Polarization-resolved study of high harmonics from bulk semiconductors. *Phys. Rev. Lett.* **120**, 243903 (2018).
88. Sekiguchi, F. et al. Enhancing high harmonic generation in GaAs by elliptically polarized light excitation. *Phys. Rev. B* **108**, 205201 (2023).
89. Goncharov, V. A. Nonlinear optical response in solids from time-dependent density-functional theory simulations. *J. Chem. Phys.* **139**, 084104 (2013).
90. Uemoto, M., Kuwabara, Y., Sato, S. A. & Yabana, K. Nonlinear polarization evolution using time-dependent density functional theory. *J. Chem. Phys.* **150**, 094101 (2019).
91. Vignale, G. & Kohn, W. Current-dependent exchange-correlation potential for dynamical linear response theory. *Phys. Rev. Lett.* **77**, 2037–2040 (1996).
92. Berger, J. A., Romaniello, P., van Leeuwen, R. & de Boeij, P. L. Performance of the Vignale-Kohn functional in the linear response of metals. *Phys. Rev. B* **74**, 245117 (2006).
93. Dinh, P. M., Lacombe, L., Reinhard, P.-G., Suraud, É. & Vincendon, M. On the inclusion of dissipation on top of mean-field approaches. *Eur. Phys. J. B* **91**, 246 (2018).
94. D'Agosta, R. & Vignale, G. Non-v-representability of currents in time-dependent many-particle systems. *Phys. Rev. B* **71**, 245103 (2005).
95. Lacombe, L. & Maitra, N. T. Non-adiabatic approximations in time-dependent density functional theory: progress and prospects. *npj Comput. Mater.* **9**, 124 (2023).
96. Elliott, P., Fuks, J. I., Rubio, A. & Maitra, N. T. Universal dynamical steps in the exact time-dependent exchange-correlation potential. *Phys. Rev. Lett.* **109**, 266404 (2012).
97. Luo, K., Fuks, J. I., Sandoval, E. D., Elliott, P. & Maitra, N. T. Kinetic and interaction components of the exact time-dependent correlation potential. *J. Chem. Phys.* **140**, 18A515 (2014).
98. Ramsden, J. D. & Godby, R. W. Exact density-functional potentials for time-dependent quasiparticles. *Phys. Rev. Lett.* **109**, 036402 (2012).

99. Suzuki, Y., Lacombe, L., Watanabe, K. & Maitra, N. T. Exact time-dependent exchange-correlation potential in electron scattering processes. *Phys. Rev. Lett.* **119**, 263401 (2017).
100. Suzuki, Y., Nagai, R. & Haruyama, J. Machine learning exchange-correlation potential in time-dependent density-functional theory. *Phys. Rev. A* **101**, 050501 (2020).
101. Sato, S. A. & Rubio, A. Limitations of mean-field approximations in describing shift-current and injection-current in materials. *Phys. Rev. B* **109**, 195205 (2024).
102. Alam, D., Ud Din, N., Chini, M. & Turkowski, V. Electron-electron interactions and high-order harmonics in solids. *Phys. Rev. B* **106**, 235124 (2022).
103. Alam, D., Ud Din, N., Chini, M. & Turkowski, V. Correlation-induced generation of superharmonics in the high-order harmonic spectrum of perovskite barium titanate. *Phys. Rev. B* **110**, 205136 (2024).
104. Lively, K., Sato, S. A., Albareda, G., Rubio, A. & Kelly, A. Revealing ultrafast phonon mediated inter-valley scattering through transient absorption and high harmonic spectroscopies. *Phys. Rev. Res.* **6**, 013069 (2024).

Acknowledgements

This work was supported by JSPS KAKENHI Grant Numbers JP20K14382 and JP21H01842, the Cluster of Excellence 'CUI: Advanced Imaging of Matter'- EXC 2056 - project ID 390715994, SFB-925 "Light induced dynamics and control of correlated quantum systems" – project 170620586 of the Deutsche Forschungsgemeinschaft (DFG), and the Max Planck-New York City Center for Non-Equilibrium Quantum Phenomena. This work was also supported by MEXT Promotion of Development of a Joint Usage/ Research System Project: Coalition of Universities for Research Excellence Program (CURE) Grant Number JPMXP1323015474. We also acknowledge support from the Marie Sk{\l}odowska- Curie Doctoral Network TIMES, grant No. 101118915, and SPARKLE grant No. 101169225; the Italian Ministry of University and Research (MUR) under the PRIN 2022 Grant No 2022PX279E_003; Next Generation EUPartenariato Esteso NQSTI - Spoke 2 (THENCE-PE00000023). The Flatiron Institute is a division of the Simons Foundation. This work used computational resources of the HPC systems at the Max Planck Computing and Data Facility (MPCDF), and the Fujitsu PRIMERGY CX400M1/CX2550M5 (Oakbridge-CX) at the Information Technology Center, the University of Tokyo through the HPCI System Research Project (Project ID:hp220112).

Author contributions

S.A.S. performed the numerical simulations. H.H. and U.G. contributed to the analysis to aid in understanding the numerical results. A.R. supervised the project. All authors participated in discussions and reviewed the manuscript.

Competing interests

The authors declare no competing interests.

Additional information

Correspondence and requests for materials should be addressed to Shunsuke A. Sato, Hannes Hübener, Umberto De Giovannini or Angel Rubio.